J|A|C|S
ARTICLES
Published on Web 09/20/2006

Time-Resolved in Situ Studies of Oxygen Intercalation into $SrCoO_{2.5}$, Performed by Neutron Diffraction and X-ray Absorption Spectroscopy

Ronan Le Toquin,[†,‡] Werner Paulus,*[,†] Alain Cousson,[‡] Carmelo Prestipino,[§,||] and Carlo Lamberti[§]

Contribution from Université de Rennes 1: Sciences Chimiques de Rennes, UMR-6226 Inorganic Materials: Soft Chemistry and Reactivity of Solids, F-35042 Rennes, France, Laboratoire Léon Brillouin, CEA-CNRS, F-91191 Gif sur Yvette, France, and Department of Inorganic, Physical and Materials Chemistry, NIS Center of Excellence, and INSTM "Centro di Riferimento", University of Turin, 10125 Turin, Italy

Received May 8, 2006; E-mail: werner.paulus@univ-rennes1.fr

Abstract: Electrochemical oxidation of the antiferromagnetically ordered $SrCoO_{2.5}$, with brownmillerite-type structure, to the cubic ferromagnet $SrCoO_3$, with perovskite structure, has been investigated in situ by neutron diffraction as well as by X-ray absorption fine structure (XAFS) spectroscopy in specially designed electrochemical cells. The neutron diffraction experiments were performed twice, using two different wavelengths ($\lambda = 1.2921(2)$ and 4.74 Å) in order to better discriminate structural and magnetic changes as functions of the charge transfer. From the neutron diffraction experiments, two intermediate phases, $SrCoO_{2.75}$ and $SrCoO_{2.82\pm0.07}$, were characterized. No superstructure reflections were observed for the corresponding $SrCoO_{2.75}$ phase. Instead we observed here, for the first time, 3D oxygen ordering during an oxygen intercalation reaction, as established for $SrCoO_{2.82\pm0.07}$, which can be described as a tetragonal unit cell, related to the perovskite cell by $a \approx 2(a\sqrt{2})$ and $c \approx 2a$. The structure of this intermediate phase confirms the strongly topotactic character of the oxygen intercalation reaction. We were also able to prove, from in situ XAFS spectroscopy at the Co absorption edge, that the evolution of the Co valence state from formally +3 for $SrCoO_{2.5}$ to +4 for the final reaction product ($SrCoO_{3.0}$) does not proceed continuously but gives evidence for the formation of O^- species for stoichiometries corresponding to $SrCoO_{2.82\pm0.07}$. The use of neutrons (vs X-rays) in the diffraction experiments and the choice of the transmission (vs fluorescence) mode in the XAFS experiment guarantee that the obtained data well represent bulk and not just surface properties.

1. Introduction

Layered perovskites have been reported to undergo topotactic ion exchange and intercalation reactions at moderate temperatures, giving access to a variety of new, generally metastable phases often showing a high degree of order.[1] On the other hand, three-dimensionnal (3D) ABO_3-type perovskites, showing a dense cubic oxygen anion lattice, are naturally less favored to undergo the same type of exchange or intercalation reactions, as all diffusion processes have to pass by interstitial lattice sites, generally involving higher activation energies barriers. The introduction of regular lattice site vacancies can considerably amplify any diffusion process. A particularly interesting point is the formation of ordered vacancies in solids, as they can also be a promising synthetic tool, especially for low-temperature soft chemistry intercalation reactions, in order to create thermodynamically inaccessible metastable phases, as is the case for the $SrCoO_{3-x}$ system reported here.

$SrCoO_{3-x}$ belongs to the family of non-stoichiometric perovskites, showing high oxygen mobility even at room temperature. Only a few compounds have been reported so far that show elevated oxygen transport properties with sufficiently low activation energy at low temperatures and even at room temperature.[2,3] This makes $SrCoO_{3-x}$ a promising candidate for use in catalysis or gas sensing, or even as an oxygen membrane, e.g., in solid oxygen fuel cells.

The structure of $SrCoO_3$ is the well-known cubic-type perovskite structure, which changes to the orthorhombic brownmillerite-type structure for $SrCoO_{2.5}$.[4−7] These structural changes concur with the modification of their electronic behavior, which

[†] Université de Rennes 1.
[‡] CEA-CNRS.
[§] University of Turin.
[||] Present address: ESRF, BP 220, F-38043 Grenoble, France.

(1) Schaak, R. E.; Mallouk, T. E. *Chem. Mater.* **2002**, *14*, 1455−1471.
(2) Shao, Z. P.; Haile, S. M. *Nature* **2004**, *431*, 170−173.
(3) Paulus, W.; Heger, G.; Rudolf, P.; Schollhorn, R. *Physica C* **1994**, *235*, 861−862.
(4) (a) Wattiaux, A.; Park, J. C.; Grenier, J. C.; Pouchard, M. *C. R. Acad. Sci. Paris Ser. 2* **1990**, *310*, 1047−1052. (b) Grenier, J. C.; Wattiaux, A.; Doumerc, J.-P.; Fournes, L.; Cheminade, J.-P.; Pouchard, M. *J. Solid State Chem.* **1992**, *96*, 20−30.
(5) Bezdicka, P.; Wattiaux, A.; Grenier, J. C.; Pouchard, M.; Hagenmuller, P. *Z. Anorg. Allg. Chem.* **1993**, *619*, 7−12.
(6) Nemudry, A.; Rudolf, P.; Schöllhorn, R. *Chem. Mater.* **1996**, *8*, 2232−2238.
(7) Takeda, Y.; Kanno, R.; Takada, T.; Yamamoto, O.; Takano, M.; Bando, Y. *Z. Anorg. Allg. Chem.* **1986**, *540/541*, 259−270.

affects tremendously the magnetic and transport properties of this material. The oxidized phase $SrCoO_{3.0}$, exhibiting ferromagnetic and metallic behavior,[4,5] can be reduced to a semiconductor, $SrCoO_{2.5}$, showing antiferromagnetic ordering,[8] both phases being magnetically ordered at room temperature. The oxygen stoichiometry can be modified at elevated temperatures as a function of the oxygen partial pressure.[7] However, it has been shown that $SrCoO_{2.5}$ can also be electrochemically oxidized via a topotactic redox reaction in an aqueous alkaline electrolyte at room temperature, yielding $SrCoO_{3.0}$ as the final reaction product.[4,5] The reaction can formally be described by

$$SrCoO_{2.5} + xO^{2-} \leftrightarrow SrCoO_{2.5+x} + 2xe^{-} \quad (0 < x < 0.5) \quad (1)$$

In the following, the variable x will be used to define the evolution of the oxygen stoichiometry during the intercalation process inside the oxide phase. The oxygen stoichiometry x is related to the charge transfer of the transferred electrons (n) by the simple relation $n = 2x$. On a stoichiometric level, this reaction is completely reversible, the total charge transfer being one electron per $SrCoO_{2.5}$ formula unit. For these reasons, this system is also interesting as a rechargeable battery electrode. However, the reversibility of the reaction is not obvious from a structural point of view. The orthorhombic starting compound $SrCoO_{2.5}$ is metastable at room temperature and can indeed only be obtained by quenching from 1000 °C (in air) into liquid nitrogen.[6] Slow cooling results in a hexagonal $SrCoO_{2.5}$ phase with 2H-$BaNiO_3$-type structure. Note that the low-temperature form of $SrCoO_{2.5}$, previously attributed to a 2H-$BaNiO_3$ type, has been recently proved to correspond to an intergrowth phase corresponding to rhombohedral $Sr_6Co_5O_{15}$ and Co_3O_4 (or CoO).[7,9] The brownmillerite phase can be described as an oxygen-anion-deficient perovskite phase, and its structure can be derived from the cubic phase by releasing oxygen atoms in an ordered way along the $[110]_{cubic}$ direction. As described in Figure 1, three different prototypes of oxygen vacancy ordering have been reported so far with the stoichiometry $AMO_{2.5}$, where A is a large cation (A = Sr, La, Ca, ...) and M is a 3d transition metal cation (M = Fe, Co, Ni, Mn ...).

These three prototypes can all be obtained schematically from the perovskite structure, modifying every second octahedral layer toward lower coordination transition metal polyhedra, such as a square planar coordination in $LaNiO_{2.5}$[10] or a square-based pyramid coordination in $CaMnO_{2.5}$.[11] The brownmillerite structure is finally characterized by layers containing isolated MO_4 tetrahedral zigzag chains, alternating with octahedral layers (top part of Figure 2).[12] Vacancy ordering leads to the formation of empty 1D channels along the $[110]_{cubic}$ direction. Consequently, the symmetry becomes orthorhombic, with cell parameters $a_{brown} \approx a_{perovs}\sqrt{2}$, $b_{brown} \approx 4a_{perovs}$, and $c_{brown} \approx a_{perovs}\sqrt{2}$, but the

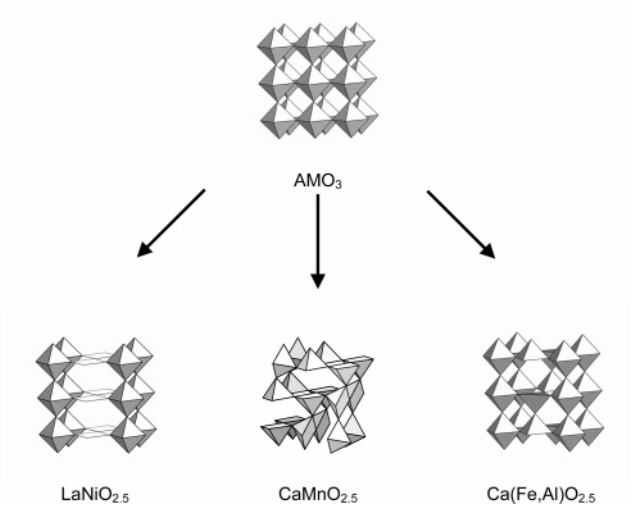

Figure 1. Schematic representation of the three prototype structures with stoichiometry $AMO_{2.5}$ obtained by reduction of the perovskite AMO_3. The three prototypes are characterized by partial or total replacement of the MO_6 octahedra in the perovskite by square planar MO_4 in $LaNiO_{2.5}$, by square pyramids MO_5 in $CaMnO_{2.5}$, and by tetrahedral MO_4 in the brownmillerite $Ca(Fe,Al)O_{2.5}$ or $SrCoO_{2.5}$.

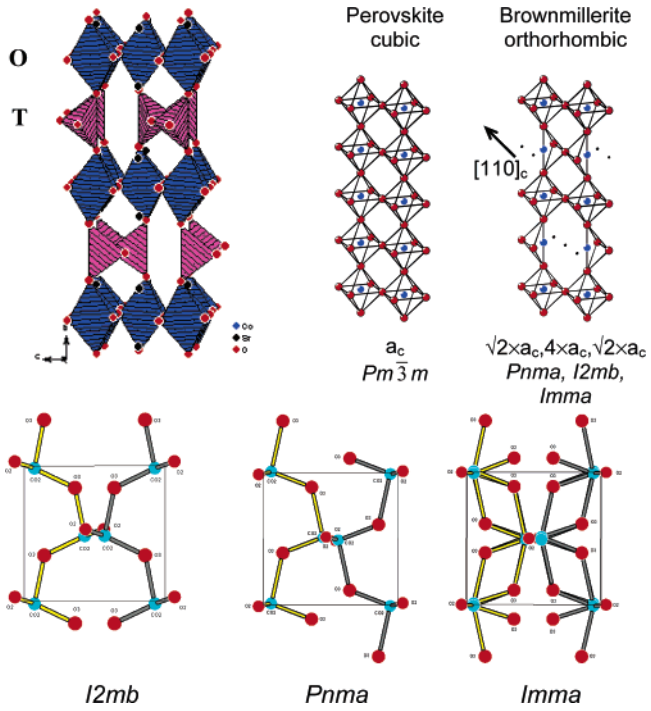

Figure 2. (Top) Structure of the brownmillerite $SrCoO_{2.5}$, showing the CoO_6 octahedral (**O**) and CoO_4 tetrahedral (**T**) layers alternating along the *b*-axis and the 1D oxygen vacancy channel parallel to $[100]_{brown} = [110]_{perovs}$ (left). Schematic representation of the transformation from the perovskite structure (middle) to the brownmillerite structure (right). (Bottom) Representation of the "zigzag" chains of CoO_4 tetrahedra in the three different space groups, *I2mb*, *Pnma*, and *Imma*, reported for brownmillerite compounds. In yellow are the CoO_4 chains parallel to the *a*-axis at $y = 1/4$. In red are the chains at $y = 3/4$ deduced from the ones at $y = 1/4$ by a mirror in *I2mb*, a center of inversion in *Pnma*, and the combination of both in *Imma*. For clarity, only one chain per layer is outlined.

attribution of the space group remains ambiguous between *Pnma*, *Imma*, and *I2mb*. The first structure determination of the brownmillerite mineral, $Ca(Fe,Al)O_{2.5}$, has revealed space group *Pnma*.[13] P-type reflections $h + k + l = 2n + 1$, although characterized by a very low intensity, have been clearly

(8) Takeda, T.; Yamaguchi, Y.; Watanabe, H. *J. Phys. Soc. Jpn.* **1972**, *33*, 970−972.
(9) (a) Harrison, W. T. A.; Hegwood, S. L.; Jacobson, A. J. *J. Chem. Soc., Chem. Commun.* **1995**, 1953−1954. (b) Zakhour-Nakhl, M.; Weill, F.; Darriet, J.; Perez-Mato, J. M. *Int. J. Inorg. Mater.* **2000**, *2*, 71−79.
(10) (a) Vidyasagar, K.; Reller, A.; Gopalakrishnan, J.; Rao, C. N. R. *J. Chem. Soc., Chem. Commun.* **1985**, 7−8. (b) Alonso, J. A.; Martinez Lope, M. J.; Garcia Munoz, J. L.; Fernandez Diaz, M. T. *J. Phys.-Condes. Matter* **1997**, *9*, 6417−6426.
(11) (a) Reller, A.; Thomas, J. M.; Jefferson, D. A.; Uppal, M. K. *Proc. R. Soc. A* **1984**, *394*, 223−241. (b) Reller, A. *J. Phys. Chem.* **1987**, *90*, 913−914.
(12) Hansen, W. C.; Brownmiller, L. T.; Bogue, R. H. *J. Am. Chem. Soc.* **1928**, *50*, 396−406.

observed. However, many other compounds $AMO_{2.5}$ have been reported to have a different symmetry, with space group *Imma* or *I*2*mb*.[14−17] The general problem is that only slight differences exist in the arrangement of the MO_4 tetrahedral chains for these three space groups (see bottom part of Figure 2). *I*2*mb* and *Pnma* refer to two different ordering schemes for the MO_4 zigzag chains, while *Imma* implies a statistical disorder of MO_4 tetrahedra, which is approximately equivalent to a coherent mixing of *Pnma* and *I*2*mb* domains. Some compounds of the brownmillerite type show a certain degree of order within the MO_4 planes.[16] The possible presence of both domain phases and different kinds of disorder, such as stacking faults or possible formation of antiphase domains in the tetrahedral layers, make it impossible to easily discriminate among these different space groups. The real structure of most brownmillerite-type compounds, and especially $SrCoO_{2.5}$, is not yet known in detail.

Oxygen vacancy ordering is also not fully understood in the isostructural $SrFeO_{2.5}$. For this phase, oxygen vacancy ordering has been proven by Mössbauer spectroscopy even 120 K above the orthorhombic-to-cubic phase transition at $T = 1103$ K.[18] However, the MO_4 ordering in $AMO_{2.5}$ structures seems to play a crucial role in the chemical reactivity, since ordered brownmillerite-type phases with space group *Pnma*, such as $CaFeO_{2.5}$, are not able to intercalate oxygen by electrochemical oxidation. This might lead to the more or less general conclusion that oxygen intercalation at room temperature is strongly limited to disordered and most probably dynamically disordered MO_4 tetrahedral chains. Therefore, $SrCoO_{2.5+x}$ must be considered as a key system for the understanding of low-temperature reaction mechanisms with oxygen diffusion, as it exhibits a particular high charge transfer of $n = 1$. Concerning the reaction mechanism, it would be very important to know the mechanism by which the oxygen intercalation proceeds, i.e., whether the topotactic uptake of oxygen atoms involves ordered or disordered intermediate phases, even on a local level. This point is important also with respect to the tailoring of new compounds with high oxygen ion conductivity, especially at low temperatures.

For this reason, the structural characterization of the order/disorder phenomena in the tilting arrangement of the tetrahedral layers is a key step in the understanding of the high oxygen mobility at room temperature. It is also crucial to know whether, at the end of the oxidation/reduction cycle, the stoichiometric $SrCoO_{2.5}$ phase still reflects the structural disorder of the native phase obtained by quenching from high temperatures. An alternative model would be the generation of an ordered phase, now resulting from the electrochemical reduction of cubic $SrCoO_{3.0}$ at ambient temperature, i.e., far away from thermodynamic equilibrium.

The $SrCoO_{2.5} \leftrightarrow SrCoO_3$ reaction mechanism has been investigated by in situ X-ray diffraction on polycrystalline electrodes,[6] revealing a high complexity and involving also intermediate phases. According to Nemudry et al.,[6] the oxidation of $SrCoO_{2.50}$ leads directly to $SrCoO_{2.75}$, which is assumed to be a cubic phase. A second phase, nominally $SrCoO_{2.875}$, has been observed, and the associated specific peak broadening suggests a tetragonal symmetry. The general problem encountered when investigating solid-state reactions by in situ X-ray diffraction methods is that, due to absorption phenomena, one can examine only the upper ~ 20 μm of the sample. This may result in real problems for the correlation of the applied charge transfer and structural changes, as the generally observed slow reaction kinetics for solid-state processes may yield inhomogeneities between the surface and the bulk of the working electrode. Furthermore, the relatively low sensitivity of X-rays toward oxygen atoms is a limiting factor in observing possible intermediate phases.

Despite the great interest in these systems for future applications, no structural description of the real structure has been proposed for $SrCoO_{2.5+x}$ phases, in order to explain the high chemical reactivity and the diffusion mechanism of the oxygen atoms.

Taking into account these different points, our reason for reinvestigating the reaction mechanism now by in situ neutron diffraction techniques is threefold: first, we want to verify that the results reported in refs 4−6 are real bulk effects. Our second aim is to follow simultaneously the evolution of the nuclear and magnetic structures during the electrochemical oxidation of $SrCoO_{2.5}$, which are both directly accessible by neutron diffraction. Finally, the better sensitivity of neutron diffraction toward (low-*Z*) oxygen atoms will favor the detection and characterization of any intermediate phase, related to the ordering of the oxygen atoms.

Besides the diffraction studies, we have also focused on understanding the local changes in the partially disordered phase. In particular, we wanted to find out more about the evolution of the valence state and local environnement of the Co atoms on a more local level using in situ X-ray absorption fine structure (XAFS) spectroscopy during the electrochemical oxidation. The high photon flux, now available at third-generation synchrotron radiation sources, has made it possible to follow, in real time with X-ray absorption techniques in transmission mode, catalytic[19−23] or electrochemical reactions[24] with a reasonable time resolution. Therefore, we used X-ray absorption spectroscopy to study the oxidation and aggregation changes occurring during a solid-state intercalation reaction carried out in situ in

(13) Bertaut, E. F.; Blum, P.; Sagnières, A. *Acta Crystallogr.* **1959**, *12*, 149−159.
(14) Hodges, J. P.; Short, S.; Jorgensen, J. D.; Xiong, X.; Dabrowski, B.; Mini, S. M.; Kimball, C. W. *J. Solid State Chem.* **2000**, *151*, 190−209.
(15) Hardner, M.; Müller-Buschbaum, H. *Z. Anorg. Allg. Chem.* **1980**, *464*, 169−175.
(16) (a) Abakumov, A. M.; Rozova, M. G.; Pavlyuk, B. P.; Lobanov, M. V.; Antipov, E. V.; Lebedev, O. I.; Van Tendeloo, G.; Sheptyakov, D. V.; Balagurov, A. M.; Bouree, F. *J. Solid State Chem.* **2001**, *158*, 100−111. (b) Abakumov, A. M.; Rozova, M. G.; Pavlyuk, B. P.; Lobanov, M. V.; Antipov, E. V. *J. Solid State Chem.* **2001**, *160*, 353−361.
(17) Colville, A. A. *Acta Crystallogr. B* **1970**, *26*, 1469−1473.
(18) Takano, M.; Okita, T.; Nakayama, N.; Bando, Y.; Takeda, Y.; Yamamoto, O.; Goodenough, J. B. *J. Solid State Chem.* **1988**, *73*, 140−150.
(19) Haas, O.; Holzer, F.; Muller, S.; McBreen, J. M.; Yang, X. Q.; Sun, X.; Balasubramanian, M. *Electrochim. Acta* **2002**, *47*, 3211−3217.
(20) Lamberti, C.; Bordiga, S.; Bonino, F.; Prestipino, C.; Berlier, G.; Capello, L.; D'Acapito, F.; Llabrés i Xamena, F. X.; Zecchina, A. *Phys. Chem. Chem. Phys.* **2003**, *5*, 4502−4509.
(21) Prestipino, C.; Berlier, G.; Llabrés i Xamena, F. X.; Spoto, G.; Bordiga, S.; Zecchina, A.; Turnes Palomino, G.; Yamamoto, T.; Lamberti, C. *Chem. Phys. Lett.* **2002**, *363*, 389−396.
(22) Llabrés i Xamena, F. X.; Fisicaro, P.; Berlier, G.; Zecchina, A.; Turnes Palomino, G.; Prestipino, C.; Bordiga, S.; Giamello, E.; Lamberti, C. *J. Phys. Chem. B* **2003**, *107*, 7036−7044.
(23) Lamberti, C.; Prestipino, C.; Bonino, F.; Capello, L.; Bordiga, S.; Spoto, G.; Zecchina, A.; Diaz Moreno, S.; Cremaschi, B.; Garilli, M.; Marsella, A.; Carmello, D.; Vidotto, S.; Leofanti, G. *Angew. Chem., Int. Ed.* **2002**, *41*, 2341−2344.
(24) (a) Deb, A.; Bergmann, U.; Cairns, E. J.; Cramer, S. P. *J. Synchrotron Radiat.* **2004**, *11*, 497−504. (b) Haas, O.; Deb, A.; Cairns, E. J.; Wokaun, A. *J. Electrochem. Soc.* **2005**, *152*, A191−A196.

an electrochemical cell on homogeneous working electrodes of 25 μm thickness.

2. Experimental Details and Methods

2.1. Synthesis and Working Electrode Preparation. $SrCoO_{2.5}$ was prepared by solid-state reaction techniques. $SrCO_3$ and Co_3O_4 were thoroughly mixed together in stoichiometric quantities and pressed into pellets of 13 mm diameter and 1 g weight, which were heated in air for 48 h at 900 and 1250 °C successively. Further annealing at 1000 °C for 6 h was performed in order to reach the stoichiometry $SrCoO_x$, with $x = 2.5$. At this temperature, the symmetry of the phase is still cubic, and fast quenching into liquid N_2 was carried out in order to induce the transformation to the orthorhombic, brownmillerite-type $SrCoO_{2.5}$. The pellets thus obtained were used as working electrodes for the electrochemical investigations as well as for the structural studies by in situ neutron powder diffraction. Although absorption was not a major problem for the neutron diffraction experiments, it turned out to be a severe handicap for the X-ray absorption experiments at the Co K-edge. For that experiment, which was performed in transmission mode, we calculated the optimum thickness of the electrodes to be about 25 μm. Therefore, they were prepared by intimate mixing of polycrystalline $SrCoO_{2.5}$ powder with 2 wt % Teflon and then pressed into homogeneous electrodes. All electrochemical cells were developed and optimized in terms of the materials, dimensions, and current densities in the laboratory. All setups were composed of an electrochemical cell containing three electrodes (working electrode, Pt counter electrode, and Ag/AgCl reference electrode) in a 1 N KOH electrolyte.

2.2. In Situ Neutron Powder Diffraction. In situ neutron powder diffraction (NPD) studies were carried out on the D20 diffractometer at the ILL at Grenoble, France, and on the G6.1 diffractometer of the ORPHEE reactor at Saclay, France. The D20 high-flux neutron powder diffractometer installed at the Institut Laue Langevin (Grenoble, France) was used at $\lambda = 1.2921(2)$ Å, in order to collect data at elevated $\sin(\theta)/\lambda$ values for high-accuracy structure analysis. The diffractometer is equipped with a large microstrip detector covering a scattering angle of 154° simultaneously. Powder patterns were collected every 25 min during 3.5 days in order to achieve a charge-transfer resolution of $\Delta n = 0.005$ electrons ($\Delta x = 0.0025$, see eq 1) per diffractogram. We also performed the same in situ experiment on the G6.1 two-axis diffractometer, installed at the ORPHEE reactor in Saclay. The very large wavelength of 4.74 Å was useful to better separate the purely magnetic doublet (120/021) and to study the evolution of magnetic changes with the charge transfer. The diffractometer is equipped with a 1D detector covering 80° (2θ). The electrochemical cells used for in situ neutron diffraction were totally made of quartz, as it is quite transparent for neutrons, keeping the background to a reasonable scale. The 1 N KOD electrolyte was prepared from equivalent amounts of 40% KOD solution in D_2O (99.9% enriched, Aldrich) and D_2O (99.9% enriched, Eurisotop). The fresh electrolyte was pumped at constant flow through the electrochemical cell, in order to guarantee stable reaction conditions, and also to obtain a constant background during the whole experiment. The cell was equipped with a platinum counter electrode and a Ag/AgCl reference electrode, as described in detail elsewhere.[25] All electrochemical oxidation reactions were carried out in galvanostatic reaction mode, i.e., applying a constant current. The applied current density did not exceed 500 μA/cm^2.

2.3. Synchrotron X-ray Powder Diffraction (XRPD). The Swiss−Norwegian powder diffractometer (BM01B, $\lambda = 0.5000(1)$ Å) installed at the European Synchrotron Research Facility in Grenoble (ESRF) was used to characterize the intermediate phases obtained ex situ. Measurements were performed at room temperature. A Si(111) double-crystal monochromator was used to select the wavelength from the white beam. An array of six scintillation counters was mounted in order to increase the statistics, since all six counts are added for a given 2θ value. To reach high resolution, a Si(111) single crystal was mounted in front of each detector.

2.4. In Situ X-ray Absorption Spectroscopy. High-resolution X-ray absorption experiments were performed at the Co K-edge in transmission mode at the BM29 beam-line[26] of the ESRF using a Si(111) monochromator, detuned up to 1/3 to reject harmonics. To guarantee an exact energy calibration, the following experimental setup was adopted: (i) the intensity of the monochromatic beam, $I_0(E)$, was measured in a first ionization chamber; (ii) the monochromatic beam was partially absorbed while crossing the sample of thickness x; (iii) the intensity of the transmitted beam, $I_1(E)$, was then measured in a second ionization chamber; (iv) the remaining beam was further absorbed by passing through a Co metal foil reference sample of thickness x_R; and (v) the intensity of the beam transmitted by the reference sample, $I_2(E)$, was finally measured in a third ionization chamber. In such a way, the absorption coefficients of the sample (μ) and of the reference (μ_R) can be measured for a given energy E selected by the monochromator according to the classical law of transmission phenomena: $\mu(E)x = \ln[I_0(E)/I_1(E)]$ and $\mu_R(E)x_R = \ln[I_1(E)/I_2(E)]$.[20] Small fluctuations in the angle/energy relationship of the monochromator due to thermal instabilities of the silicon crystals and/or to beam fluctuations can be (if needed) corrected a posteriori. Such cautions are of primary importance when one wants to follow the evolution of the oxidation state of a transition metal during a solid-state redox reaction.[20−22] The X-ray absorption near-edge structure (XANES) region was acquired with a sampling step of 0.3 eV, while the extended X-ray absorption fine structure (EXAFS) region was acquired up to 13 Å^{-1} with a constant sampling step, in k-space, of 0.025 Å^{-1}. X-ray absorption measurements were acquired in situ during the electrochemical reaction using a test cell optimized to minimize the thickness of the solution, which is highly absorbing at the Co K-edge, crossed by the beam.

Under the adopted conditions, a single X-ray absorption spectrum (including both high-resolution XANES and EXAFS) requires slightly less than 40 min. This time is inclusive of the time spent to move back the monochromator below the Co K-edge to start the acquisition of the next spectrum. The current was set to perform the complete $SrCoO_{2.5} \rightarrow SrCoO_{3.0}$ oxidation in 2500 min. This allows more than 60 spectra to be collected during the reaction. Within a single spectrum, the charge transfer n was 0.016 electron/formula unit (corresponding to $\Delta x = 0.008$), a sufficiently low value to consider the sample almost unchanged between the first and the last sampled points of a single spectrum.

2.5. Structure Refinements. Structure refinements of all NPD data were undertaken by FULLPROF;[27] the values taken for the neutron scattering lengths for the respective elements are $b_{Co} = 2.49$ fm, $b_{Sr} = 7.02$ fm, and $b_O = 5.805$ fm.[28] Special care was taken in the background correction of the in situ experiment on D20. The background was carefully determined from the fully oxidized phase $SrCoO_3$, as it contains fewer reflections, and was taken as constant for the whole experiment.

3. Results and Discussion

3.1. Evolution of the Electrochemical Potential during Intercalation. Following eq 1, the oxidation of $SrCoO_{2.5}$ to $SrCoO_3$ corresponds to a total charge transfer (n) of one electron per formula unit, corresponding to the intercalation of $x = 0.5$ oxygen atoms under the assumption that O^{2-} is the only intercalated species. In this way, the oxidation reaction can be followed on a stoichiometric level, applying a constant

(25) Paulus, W. Habilitation, University of Paris XI, 1998.

(26) Filipponi, A.; Borowski, M.; Bowron, D. T.; Ansell, S.; Di Cicco, A.; De Panfilis, S.; Itie, J. P. *Rev. Sci. Instrum.* **2000**, *71*, 2422−2432.

(27) Rodriguez-Carvajal, J.; Roisnel. T. *Fullprof98* and *Winplotr*, New windows 95/NT application for diffraction: Commission for powder diffraction. *IUCr Newsl.* **1998**, No. 20 (Summer, May−August).

(28) Koester, L.; Rauch, H.; Seymann, E. *At. Data Nucl. Data Tables* **1991**, *49*, 65−120.

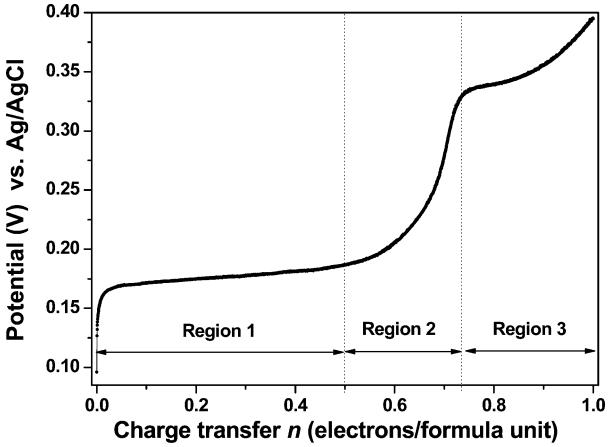

Figure 3. Evolution of the electrochemical potential (versus Ag/AgCl) as a function of the charge transfer during the intercalation of oxygen into $SrCoO_{2.5}$. The fully oxidized perovskite phase $SrCoO_{3.0}$ is obtained after the transfer of 1 electron/formula unit. The trend of the potential curve suggests the presence of three different regions, the first one showing an almost constant potential.

current. For ceramic oxides, the completeness of the reaction and the reproducibility of the potential are generally limited by contact problems between the grains of the polycrystalline working electrode. In the case of $SrCoO_{2.5}$ this problem is even more pronounced, as a volume shrinkage of about 5% occurs during the oxidation to $SrCoO_3$. Satisfying results were obtained using either the as-sintered pellets of about 13 mm diameter and 1 mm thickness or ultrathin pressed electrodes, optimized for neutron diffraction and XAFS experiments, respectively.

The electrochemical potential (Figure 3) shows mainly three different regions. The first region ($0 \leq n \leq 0.5$) shows a potential plateau at about $V = 175$ mV. After the exchange of 0.5 electron, we observe in region 2 a steep increase of V up to 330 mV, reached around $n = 0.75$. Region 3 ($0.75 < n < 1.00$) exhibits a more or less continuous increase of the potential to about 400 mV. Further oxidation then leads to the formation of molecular oxygen from water decomposition at the anode. Although the reaction is principally entirely reversible, the first reduction of the $SrCoO_3$ polycrystalline electrodes showed a decreased charge transfer of approximately 10−15% that accumulates with the number of oxidation/reduction cycles. In terms of oxygen stoichiometry, the electrochemical phase diagram is composed of a two-phase reaction from $SrCoO_{2.5}$ to $SrCoO_{2.75}$, followed by a one-phase reaction step to $SrCoO_{2.875}$. In the third region, continuous oxidation leads homogeneously to the final reaction product, $SrCoO_3$.

3.2. In Situ Neutron Diffraction Studies. Time-resolved neutron powder diffraction (NPD) patterns measured in situ during the electrochemical oxidation (D20 with $\lambda = 1.2921(2)$ Å) are shown in Figure 4. The reaction was performed in a galvanostatic mode, which allows direct correlation of the structural and magnetic evolutions with the charge transfer. According to the pattern evolution, the progressive decrease in the intensity of the reflections of the $SrCoO_{2.5}$ phase and the appearance of new peaks clearly confirm that the browmillerite phase $SrCoO_{2.5}$ directly transforms in a biphasic reaction step into a "deficient perovskite structure" with $SrCoO_{2.75}$ stoichiometry. This fact agrees well with the almost constant value of the electrochemical potential in region 1 (see Figure 3).

From our NPD data, no evidence of reflection broadening was observed. Every reflection belonging to the oxygen-deficient perovskite phase and appearing in the first half of the reaction can be indexed with a simple cubic perovskite unit cell. Consequently, we assume for this growing intermediate phase, $SrCoO_{2.75}$, and also for all phases with higher oxygen content, referred to as "oxygen-deficient perovskite phases" in the first step, an average cubic symmetry.

We will discuss first (section 3.2.1) the results of the Rietveld refinements obtained from the NPD patterns collected in region 1 ($0.0 < n < 0.5$) and successively (section 3.2.2) those concerning regions 2 and 3 ($0.5 < n < 1.0$). This exposition plan implies that Figure 5, reporting simultaneously data on the whole $0.0 < n < 1.0$ range, will be anticipated in section 3.2.1, where only the results concerning the first region will be discussed. The remaining part of the data will be commented on in section 3.2.2.

3.2.1. Details on the $0 < n < 0.5$ Region. For the NPD refinements, we used the nuclear and magnetic structure model of $SrCoO_{2.5}$ in *Pnma*. For the intermediate phase, $SrCoO_{2.75}$, we used, in a first approximation, the cubic perovskite symmetry with space group $Pm\bar{3}m$ with a fixed oxygen stoichiometry. The two phases were refined simultaneously on the basis of the Rietveld refinement technique that allows the evolution of all parameters, especially their scale factors, to be followed separately. The refined scale factors of the two phases both show a linear evolution as a function of the charge transfer, as depicted in Figure 5a. For $0.0 < n < 0.5$, the scale factor of the starting phase decreases linearly with the charge transfer to zero, while that of the oxygen-deficient perovskite increases linearly yielding, within the given error bars, a constant sum, which was not constrained during the refinement. After a charge transfer of $n = 0.5$ electron (i.e., $x = 0.25$), the brownmillerite phase has totally disappeared, yielding only the oxygen-deficient perovskite $SrCoO_{2.75}$. The fact that the scale factors found for the starting compound (at $n = 0$) and for the intermediate cubic phase (at $n = 0.5$, see Figure 5a) are identical shows that no significant amorphous phase is formed during the intercalation reaction and also that the whole compound has reacted. As shown in Figure 5b, the lattice parameters of the orthorhombic brownmillerite phase ($a = 5.448(5)$ Å, $b = 15.738(8)$ Å, and $c = 5.545(4)$ Å) and the $SrCoO_{2.75}$ intermediate phase ($a = 3.842(2)$ Å) are observed to be constant for $0.0 < n < 0.5$. This result confirms the biphasic reaction mechanism during the first half of the reaction, as previously suggested on the basis of the evolution of the electrochemical potential (see Figure 3). The cubic cell parameter of the oxygen-deficient perovskite is larger than the value $a = 3.830$ Å observed for the fully oxidized perovskite, $SrCoO_{3.0}$.[4−8] This is consistent with the smaller average valence state of cobalt in this oxygen-deficient perovskite, which leads to a larger average Co−O distance. Direct evidence of these facts comes also from the in situ XAFS study (see section 3.6).

Figure 5c shows the evolution of the integrated intensity of the most characteristic reflections of the two phases as a function of the charge transfer, n. In the $0 < n < 0.5$ region, the linear decrease of the intensity of the (020) reflection for the $SrCoO_{2.5}$ phase, accompanied by the linear increase of the intensity of the (200) reflection of the $SrCoO_{2.75}$ phase, testifies, once again,

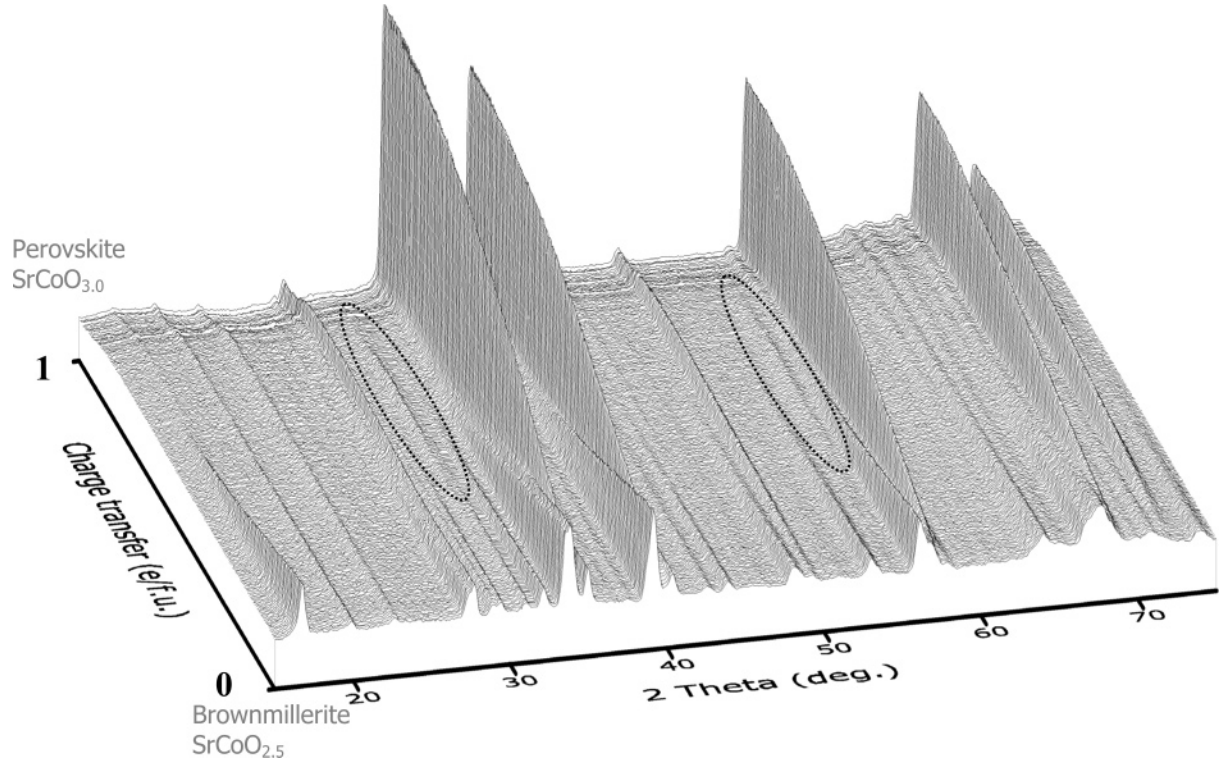

Figure 4. Evolution of the NPD pattern obtained in situ during the electrochemical oxidation of $SrCoO_{2.5}$ vs charge transfer. The diffractogram of the brownmillerite $SrCoO_{2.5}$ is represented at the bottom, whereas that of the perovskite $SrCoO_{3.00}$ is shown at the top. The dotted ellipsoids show the positions of the superstructure reflections.

to the progressive transformation of the brownmillerite into the oxygen-deficient perovskite.

3.2.2. Details on the 0.5 < *n* < 1.0 Region. At $x = 0.25$ ($n = 0.50$), the starting phase $SrCoO_{2.5}$ has completely disappeared and only the oxygen-deficient perovskite phase $SrCoO_{2.75}$ persists. For all refinements beyond a stoichiometry of $SrCoO_{2.75}$, we added one additional parameter, the occupation factor of the oxygen atoms (Figure 5d), still assuming an average cubic symmetry. At the end of the oxidation run ($n = 1$), the refined oxygen occupancy results in an estimated stoichiometry of $x = 0.48$, which is very close to the ideal one ($x = 0.5$).

From the results given in Figure 5a, it becomes obvious that further oxidation does not strongly affect the scale factor. Just a slight decrease is observed at the beginning of the $0.5 < n < 0.8$ region. This may be related to the presence of the ordered intermediate phase (see below), giving rise to extra superstructure reflections. The intensity of these extra peaks does not, consequently, contribute to the volume fraction of the pure cubic phase.

As the oxygen occupation (increasing) and the lattice parameter (monotonic variation) are the only parameters that vary with the charge transfer n, the reaction appears to be monophasic. This argument goes along with the continuous increase of the electrochemical potential beyond a charge transfer of $n = 0.5$ electron (see regions 2 and 3 in Figure 3). As expected for a one-phase region, the cubic lattice parameter decreases continuously from 3.842 ($x = 0.5$) to 3.830 Å for the final phase, $SrCoO_3$ (Figure 5b). This result has to be correlated with the linear increase of the oxygen content in the average cubic perovskite unit cell (Figure 5d), causing an increase of the valence state from Co^{3+} to Co^{4+}. Both factors are consistent with the drop in the average cubic lattice parameter in the second half of the reaction.

For the reflections of the oxygen-deficient perovskite phase, the evolution of the intensity with respect to the oxygen stoichiometry can be easily deduced from the calculation of their structure factors. This is related to the additional contribution of the intercalated oxygen to the structure amplitude F_{hkl}, which can be written as

$$F_{hkl} \propto b_{Co} + b_{Sr}(-1)^{(h+k+l)} + \xi_O[b_O(-1)^h + b_O(-1)^k + b_O(-1)^l] \quad (2)$$

Here, b_{Co}, b_{Sr}, and b_O are the neutron scattering lengths of the respective elements (see section 2.5) and ξ_O is the oxygen site occupancy factor. The refinement is very sensitive to ξ_O because different types of reflections exhibit either an increase or a decrease of the intensity upon oxygen intercalation. As an example, (eee) and (uuu) reflections (e = even, u = uneven) show an increase for the corresponding F when changing from $SrCoO_{2.75}$ to $SrCoO_3$, whereas (euu) reflections show the opposite trend. In this regard, it is worth noting that the linear increase of the intensity of the (200) reflection of the oxygen-deficient perovskite phase, observed in Figure 5c for $n > 0.5$, reflects the modulation of its structure factor amplitude by ξ_O, as $F_{(200)}$ is directly proportional to the sum of $b_{Co} + b_{Sr} + \xi_O$-$[3b_O]$ (see eq 2). This trend has a different slope than the similar one observed in the $0.0 < n < 0.5$ region, where we were dealing with the progressive formation of a new phase, characterized by a constant $F_{(200)}$ value. From these findings, we can also exclude an alternative intercalation mechanism, proposed elsewhere,[6] which would imply the intercalation of

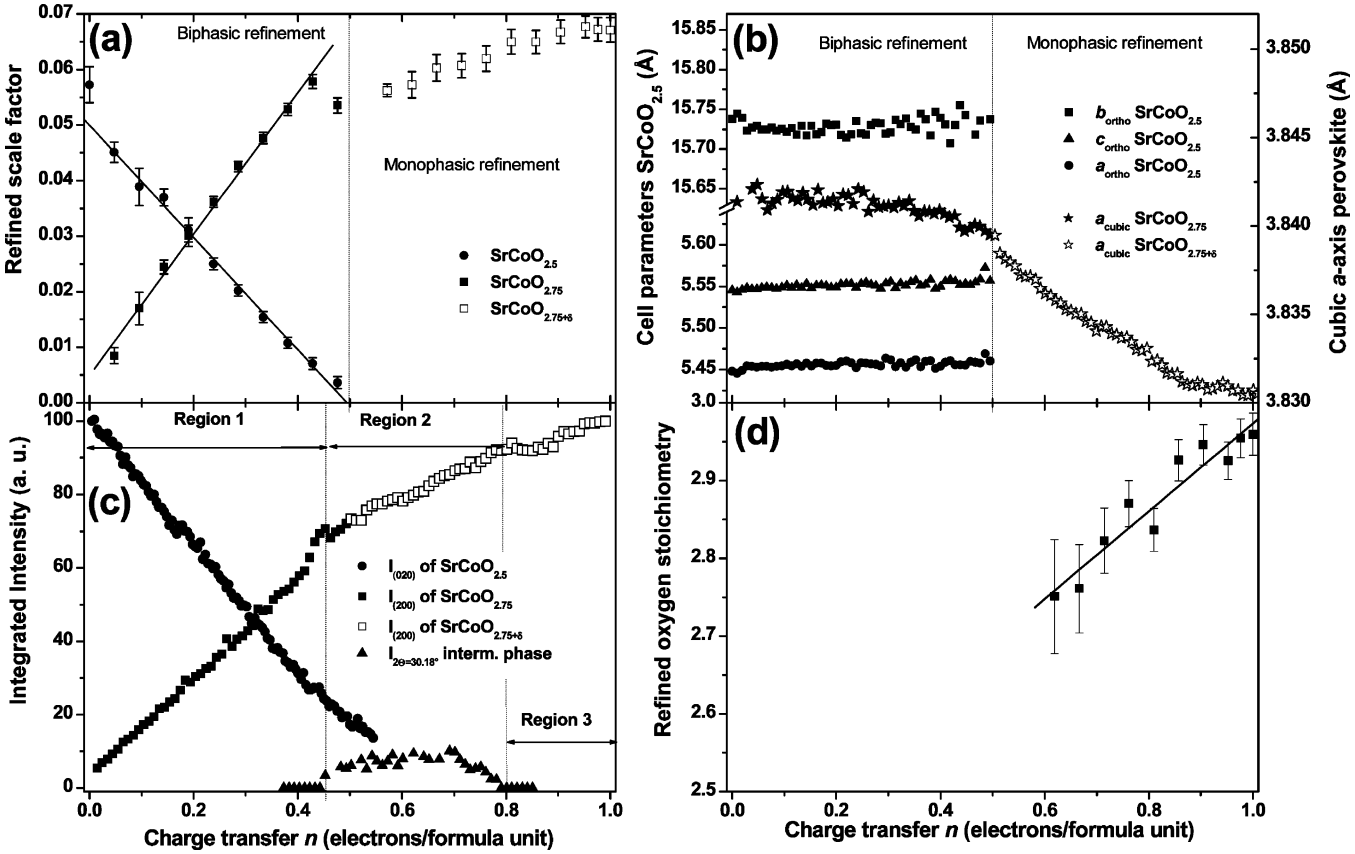

Figure 5. (a) Evolution of the refined scale factor parameters (and corresponding estimated error bars) as a function of the charge transfer *n*. In the $0 < n < 0.5$ region, a biphasic refinement has been done: full dots refer to the starting phase $SrCoO_{2.5}$, while full squares refer to the oxygen-deficient perovskite with fixed $SrCoO_{2.75}$ stoichioimetry. Lines represent the linear best fits of the data for the two phases. In the $0.5 < n < 1.0$ region, a monophasic refinement has been done for the "cubic" $SrCoO_{2.75+\delta}$ phase with a refined site occupancy factor of the oxygen position (see part (d)). (b) Evolution of the unit cell parameters as a function of the charge transfer *n*. In the $0 < n < 0.5$ region, a biphasic refinement has been done: the corresponding unit cell parameters are shown as full circles, triangles, and squares for the *a*, *b*, and *c* parameters of the orthorhombic brownmillerite phase ($SrCoO_{2.5}$, left ordinate axis) and as full stars for the cubic, oxygen-deficient perovskite phase with fixed $SrCoO_{2.75}$ stoichiometry (right ordinate axis). In the $0.5 < n < 1.0$ region, a monophasic refinement has been done for the cubic $SrCoO_{2.75+\delta}$ phase, where the site occupancy factor of the oxygen has been optimized (see part (d)). The corresponding *a* parameter is shown as open stars (right ordinate axis). (c) Evolution of the integrated intensity of characteristic reflections as a function of the charge transfer *n*: (020) for the brownmillerite $SrCoO_{2.5}$ (●), (200) for the oxygen-deficient perovskite ($SrCoO_{2.75}$, ■, for $n < 0.5$, and $SrCoO_{2.75+\delta}$, □, for $n > 0.5$), and the reflection at $2\theta = 30.18°$ for the intermediate phase (▲). For clarity, the intensity of the superstructure reflection has been multiplied by 3 (with respect to the brownmillerite intensities). (d) Evolution of the total O stoichiometry as a function of the charge transfer *n* in the $0.5 < n < 1.0$ region of the oxygen-deficient perovskite phase $SrCoO_{2.75+\delta}$. The oxygen stoichiometry was deduced from the O site occupancy factor ξ_O (see eq 2), obtained from the Rietveld analysis.

OH^- instead of O^{2-} and the formation of a $SrCoO_{2.5}(OH^-)$ phase, corresponding to an electron transfer of $n = 0.5$.

3.2.3. Intermediate Ordered Phase: $0.5 < n < 0.8$ Region. The most exciting feature observed during the oxidation is the appearance of new superstructure reflections in the region $0.5 \leq n \leq 0.8$ (see Figure 4), the strongest being at $2\theta = 30.18°$ and 36.16°, corresponding to $d = 2.48$ and 2.08 Å, respectively. The intensities of the superstructure reflections, reaching up to 4% of the intensity of the strongest basic reflection of the brownmillerite phase, i.e., the (020) reflection, are plotted as functions of the charge transfer and oxygen stoichiometry in Figure 5c. These additional reflections are certainly not of magnetic origin, as they have also been observed ex situ by X-ray synchrotron diffraction (see section 3.3 for more details), and they were observed on D20 with almost uniform intensities up to 0.4 $Å^{-1}$ in $\sin(\theta)/\lambda$, signifying indeed the ordering of the intercalated oxygen atoms. This is the first time that a 3D long-range ordering of the oxygen sub-lattice has been observed during an electrochemical oxygen intercalation reaction proceeding at room temperature. This means that, even at low temperatures, i.e., far away from thermodynamical equilibrium, the oxygen sub-lattice can relax toward new 3D ordered frameworks. Therefore, it is worth noting that $SrCoO_{2.75}$ is structurally very close to a dense cubic-packed lattice, in which any oxygen mobility at low temperature should be extremely hindered. The intensity variation of the superstructure reflections as a function of the charge transfer is given in Figure 5c, showing that the ordered phase appears at a stoichiometry of nominally $SrCoO_{2.75}$ and disappears at about $SrCoO_{2.875}$. The question of which kind of oxygen ordering can be attributed to this intermediate phase is rather difficult to answer, as is obvious; with just a few weak superstructure reflections, a structure solution by classical methods is quite impossible. Our approach was therefore to compare the intensities found for $SrCoO_{2.82\pm0.07}$ with those of oxygen ordered phases found for the homologous $SrFeO_x$ system. For the compound series $Sr_mFe_mO_{3m-1}$, two intermediate phases were characterized apart from the terminal phases with $m = 2$ and ∞ by NPD.[14,29] These intermediate phases with $m = 4$ and $m = 8$, which were synthesized at elevated temperatures under defined oxygen

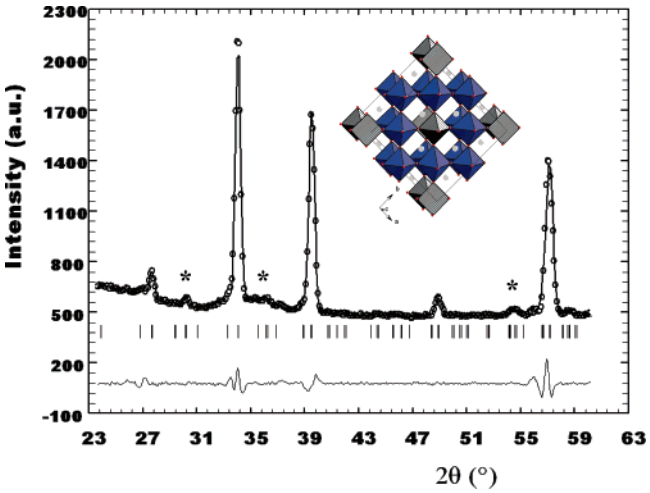

Figure 6. Observed (scattered circles) and refined (full line) diffraction profiles of the ordered intermediate phase $SrCoO_{2.82\pm0.07}$ obtained in situ by NPD. The experimental pattern corresponds to the $n = 0.64$ pattern in the series reported in Figure 4. The approach used in the structural refinement of $SrCoO_{2.82}$ was to take the structural model[14] proposed for $SrFeO_{2.875}$ in the *I*4/*mmm* space group (see the table in the Supporting Information), placing Co at the proposed Fe sites, and refining only the lattice parameters, peak line shapes, and background parameters. The superstructure reflections are marked with asterisks. The lattice parameters have been refined to $a = b = 10.862(2)$ Å and $c = 7.666(3)$ Å, and the profile reliability values are $R_p = 13.6\%$, $R_{wp} = 10.0$, and $\chi^2 = 9.11$. (Inset) The structural model of the tetragonal, ideally ordered $SrCoO_{2.875}$ phase in *I*4/*mmm*. In order to evidence the relation with the $SrCoO_{2.5}$ phase, showing alternating octahedral and tetrahedral layers, the structure is aligned with the [110] axis vertical. The native CoO_4 tetrahedral layers are now completed by oxygen atoms, forming rows of Co_2O_9 bipiramidal units (gray) alternating with rows of CoO_6 octahedra (blue).

partial pressure, correspond formally to $SrFeO_{2.75}$ and $SrFeO_{2.875}$.[14] For both phases, the true symmetry and structure are, however, still ambiguous due to the subtle oxygen ordering, leading to unit cells which are 8 or 16 times larger than the perovskite cell. One proposed structure model for $SrFeO_{2.875}$ is related to the perovskite cell by $2a\sqrt{2} \times 2a\sqrt{2} \times 2a$ with tetragonal symmetry, the space group being *I*4/*mmm*. The main structural difference with respect to the brownmillerite-type structure is the transformation of the native FeO_4 tetrahedral layer into a layer containing rows of isolated square-planar Fe_2O_9 bipyramidal units, alternating with rows of corner-sharing FeO_6 octahedra. For $SrFeO_{2.75}$, a similar structural framework was reported, with orthorhombic symmetry, space group *Cmmm*, and a smaller unit cell related to the perovskite cell by $2a\sqrt{2} \times 2a \times a\sqrt{2}$. Compared to $SrFeO_{2.875}$, the octahedral rows in the native FeO_4 layer are here reduced to isolated units of planar Fe_2O_9 bipyramids. For a schematic view of the two structures, see Figure 7. For clarity, only the evolution of the native FeO_4 tetrahedral layers is shown.

We tried to apply these two structural models in order to refine the ordered intermediate phase observed by in situ neutron diffraction. A successful refinement was possible only in the tetragonal space group *I*4/*mmm*, as we were not able to index all superstructure reflections in the orthorhombic *Cmmm* space group of $SrFeO_{2.75}$. No extra oxygen vacancies were taken into account for the refinement of $SrCoO_{2.82}$. The structure is shown in the inset of Figure 6, and the refined cell parameter values in the *I*4/*mmm* model are $a = b = 10.862(2)$ Å and $c = 7.666(3)$ Å. Figure 6 shows the diffraction profiles of the ordered intermediate phase collected at $n = 0.64$ during the in situ NPD experiment. From analysis with Rietveld refinement, it can be seen that the superstructure reflections (see Figure 6, marked by stars) are quite nicely described in terms of both intensities and angular positions, and we may assume that the structures of $SrFeO_{2.875}$ and the intermediate phase $SrCoO_{2.82\pm0.07}$ have to be considered as isotype, the $SrCoO_{2.82}$ phase showing a nonstoichiometric character. This means that the oxidation reaction mechanism of $SrCoO_{2.5}$ at low temperature proceeds in a way similar to that described for $SrFeO_{2.5}$ at medium temperature under defined oxygen partial pressures. These findings are quite important for the understanding of the chemical reactivity under nonequilibrium conditions, i.e., low temperature by electrochemistry, as the $SrCoO_x$ system at high temperatures always tends to form a thermodynamically stable hexagonal phase with a 2H-$BaNiO_3$-type hexagonal perovskite structure.[30,31] As Fe^{4+}, which is a $3d^4$ Jahn−Teller cation, is well adapted to the C_{4v} pyramidal coordination, this is not evident in the same way for Co^{4+} in the $3d^5$ state. To some extent, we have to assume a mixing-up of the sub-band structures of oxygen and cobalt, yielding less defined valence states for both elements. However, pyramidal coordination has been found for $Co^{3+}-Co^{4+}$ mixed-valence oxides of the same family, such as $Sr_3Co_2O_{7-x}$.[32] The maximum intensity of the superstructure reflections is not, however, centered exactly at $SrCoO_{2.875}$ but is between $SrCoO_{2.75}$ and $SrCoO_{2.875}$ (Figure 5c). This indicates that the one-phase reaction step in region 2 (see Figure 3) is still accompanied by some structural disorder, at least for the end members $SrCoO_{2.75}$ and $SrCoO_{2.875}$, which do not show any superstructure intensities at all (see Figure 5c). The assumption that $SrCoO_{2.75}$, obtained from electrochemical oxidation, might not be a well-ordered compound can be arrived on the basis of the evolution of the electrochemical potential (see Figure 3), as throughout region 1 the electrochemical potential smoothly increases instead of having a constant value, as expected for an ideal two-phase reaction step. This is also indicated by the potential behavior at the border between regions 1 and 2, which is not sharp but smeared out.

Further discussion is needed to explain the absence of superstructure reflections for the $SrCoO_{2.75}$ phase. From a purely structural point of view, this phase can be easily obtained in a topotactic way via removal of O from the ideally ordered $SrCoO_{2.875}$ phase shown in the inset of Figure 6. The critical point is related to the fact that this transformation is not univocal but can be obtained in different ways. Two simple possible models are briefly discussed herein, leading to two different structures for the $SrCoO_{2.75}$ phase, as schematized in Figure 7. A first crystallographically simple solution would be to remove all oxygen atoms from the 2b position of the *I*4/*mmm* model (see the table in the Supporting Information and Figure 7d), which leads to the formation of rows of CoO_4 planar squares separated by rows of CoO_6 octahedra, as indicated in Figure

(29) Tofield, B. C.; Greaves, C.; Fender, B. E. F. *Mater. Res. Bull.* **1975**, *10*, 737−745.

(30) (a) Rodríguez, J.; González-Calbet, J. M. *Mater. Res. Bull.* **1986**, *21*, 429−439. (b) Rodriguez, J.; Gonzalez-Calbet, J. M.; Grenier, J. C.; Pannetier, J.; Anne, M. *Solid State Commun.* **1987**, *62*, 231−234.

(31) (a) Gourdon, O.; Petricek, V.; Dusek, M.; Bezdicka, P.; Durovic, S.; Gyepesova, D.; Evain, M. *Acta Crystallogr. B* **1999**, *55*, 841−848. (b) Evain, M.; Boucher, F.; Gourdon, O.; Petricek, V.; Dusek, M.; Bezdicka, P. *Chem. Mater.* **1998**, *10*, 3068−3076.

(32) Dann, S. E.; Weller, M. T. *J. Solid State Chem.* **1995**, *115*, 499−507.

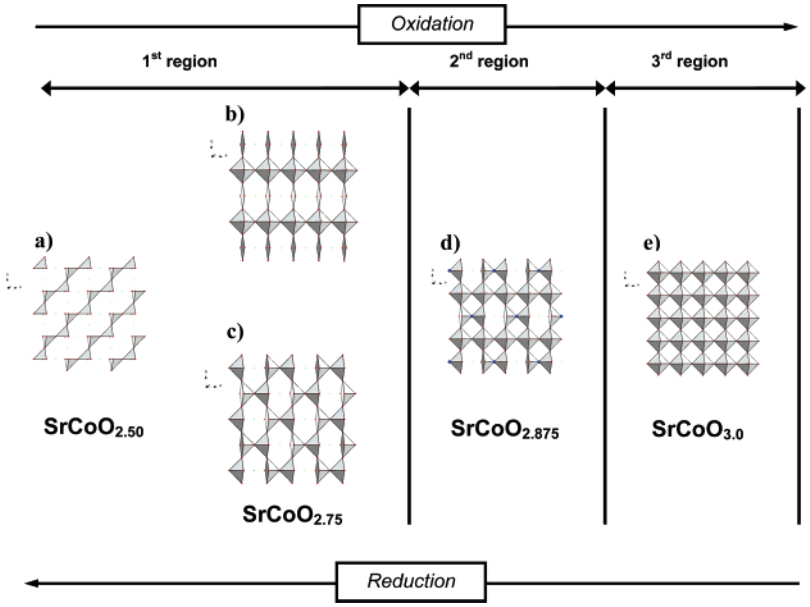

Figure 7. Model for the structural changes in the native tetrahedral layer observed during the electrochemical oxidation of $SrCoO_{2.5}$. The three different regions of the reaction are outlined. The different structural elements are designed schematically, and slight distortions are not outlined in order to allow direct comparison with the undistorted cubic perovskite $SrCoO_3$. For clarity, only one plane, hosting the native tetrahedral units of the original $SrCoO_{2.5}$ phase, is reported.

7b. A second possibility is to remove the same quantity of oxygen from the octahedral rows of the $SrCoO_{2.875}$ structure (Figure 7d), leading to the ordered model of the $SrCoO_{2.75}$ phase schematized in Figure 7c, characterized by rows of isolated Co_2O_9 square bipyramidal units, as found for the homologous $SrFeO_{2.75}$ phase in *Cmmm*.[14]

The reason that no superstructure reflections are observed in the NPD study for the electrochemically obtained $SrCoO_{2.75}$ phase might, in fact, be related to the presence of the two phases represented in Figure 7b,c. They might be present simultaneously at a microscopic coherent level, causing the loss of long-range order for this stoichiometry. Of course, we cannot rule out the simultaneous presence of additional ordered intermediate phases.

3.3. Ex Situ Synchrotron Radiation XRPD Studies of the $SrCoO_{2.82}$ Phase. The hypothesis of the ordered intermediate phase $SrCoO_{2.82\pm0.07}$, refined in *I*4/*mmm*, implies indeed a tetragonal symmetry, which we were not able to confirm by the in situ neutron diffraction experiment. This may be related not only to the insufficient instrumental resolution for peak separation but also to the increased mosaicity of the phases due to the low reaction temperature and also to possible non-stoichiometry phenomena.

The determination of the crystal structure of complex solids such as non-stoichiometric oxides is a difficult task, and different sets of diffraction data, combined with the use of other techniques, may be useful.[33,34] In this work, in order to investigate the true symmetry of the intermediate phase $SrCoO_{2.82\pm0.07}$, an electrochemically prepared sample of nominally $SrCoO_{2.82}$ composition was measured ex situ on the synchrotron radiation high-resolution powder diffractometer BM01B at the ESRF. For comparison, the cubic perovskite $SrCoO_{3.00}$ was also measured under the same experimental conditions. From this additional experiment we were able to clarify two points. First, we could see that reflections indexed in the averaged cubic perovskite cell as (*h*00) or (*hh*0) are clearly separated into two distinct diffraction peaks, whereas (*hhh*) reflections turned out to be unique (see parts a, b, and c of Figure 8, where the profiles of (111), (200), and (220) reflections are shown for both phases).

The high angular resolution of synchrotron radiation XRPD data allowed us to gain knowledge about the structure obtained from NPD data, where we were not able to observe the peak splitting reflecting the weakly distorted tetragonal symmetry of the $SrCoO_{2.82}$ phase and where refinement of the lattice parameter did not allow unambiguous assignment of a non-cubic symmetry, within the error bars. The XRPD analysis clearly indicates that the symmetry of the intermediate $SrCoO_{2.82}$ phase is indeed not cubic but tetragonal, with lattice parameters corresponding to $a = b = 3.84152(5)$ Å and $c = 3.83093(6)$ Å, leading to $a = b = 10.865$ Å and $c = 7.662$ Å for the ordered *I*4/*mmm* structure. The assignment for the *a*-, *b*-, and *c*-axis lattice parameters was done taking into account the relative peak intensities, which ideally should be about 2 times larger in the case of the superimposed (200)/(020) reflection peaks compared to the unique (002) reflection.

Second, we were able to observe very small superstructure reflections (see Figure 8d), corresponding to the ones already observed, e.g., at $d = 2.48$ and 2.08 Å during the in situ NPD experiment (see Figure 4). This supports, on one side, the correctness of the $2a\sqrt{2} \times 2a\sqrt{2} \times 2a$ superstructure unit cell, but it also underlines the non-magnetic origin of the superstructure reflections found by neutron diffraction.

3.4. Concluding Remarks on the Structural Changes Occurring during the Electrochemical Oxidation. The topotactic uptake of oxygen in the tetrahedral CoO_4 layer can then resume, as illustrated schematically in Figure 7. The separation into three sections corresponds to regions 1, 2, and 3 of the

(33) Garcia-Martin, S.; Alario-Franco, M. A.; Ehrenberg, H.; Rodriguez-Carvajal, J.; Amador, U. *J. Am. Chem. Soc.* **2004**, *126*, 3587−3596.
(34) Cussen, E. J.; Rosseinsky, M. J.; Battle, P. D.; Burley, J. C.; Spring, L. E.; Vente, J. F.; Blundell, S. J.; Coldea, A. I.; Singleton, J. *J. Am. Chem. Soc.* **2001**, *123*, 1111−1122.

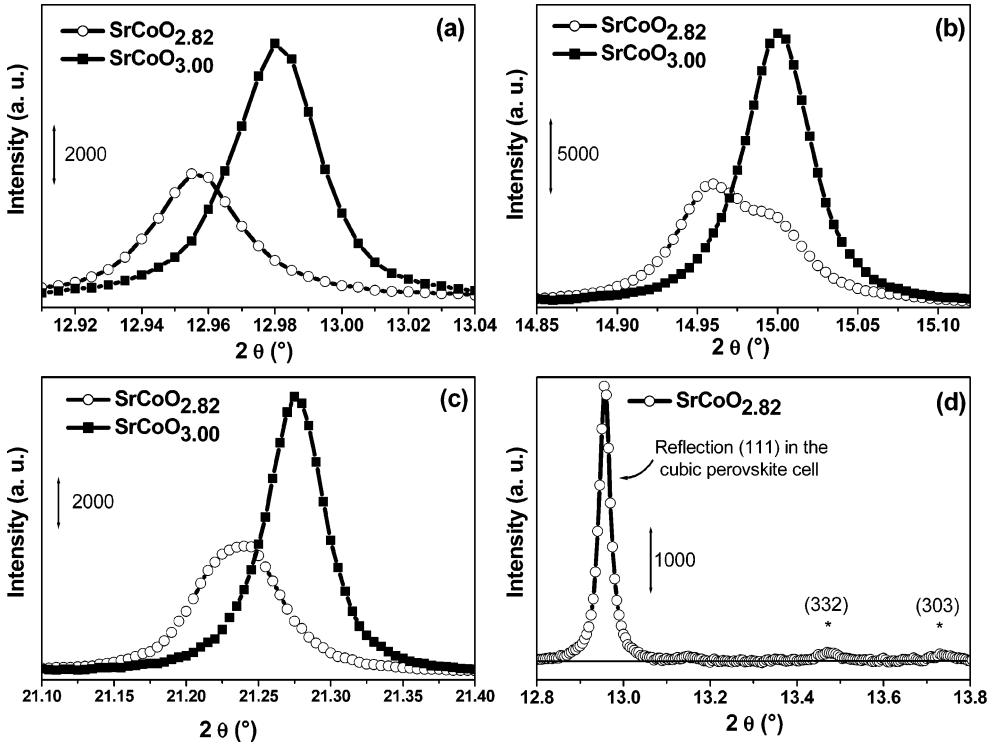

Figure 8. Comparison of the reflection profiles (111), (200), and (220) between the perovskite $SrCoO_{3.00}$ (full squares) and the intermediate phase $SrCoO_{2.82}$ (open circles), parts (a), (b), and (c), respectively. Powder patterns have been measured using X-ray synchrotron diffraction at the beamline SNBL BM01B installed at the ESRF. (d) The weak superstructure reflections ($d = 2.48$ and 2.08 Å), marked by stars, already observed in the in situ NPD experiment (see Figure 4). The index of the stronger reflection on the left side (d) is (111) with respect to the cubic perovskite unit cell, or (402) in the *I*4/*mmm* unit cell. Asterisks mark the superstructure reflections indexed (332) and (303) in the *I*4/*mmm* cell.

potential curve obtained during the electrochemical oxidation (see Figure 3). $SrCoO_{2.5}$ (Figure 7a) transforms topotactically, in a two-phase reaction step, into $SrCoO_{2.75}$ (Figure 7b,c). As no long-range order has been observed for this phase, we have to assume a coherent mixing of the two ordered phases containing (in the planes of the native CoO_4 tetrahedra) simultaneously CoO_6 octahedra and square planar CoO_4 units as well as square planar bipyramidal Co_2O_9 units. The disordered $SrCoO_{2.75}$ phase then transforms, in a one-phase reaction step, into the disordered $SrCoO_{2.875}$ phase through the formation of an ordered intermediate phase stoichiometrically centered at $SrCoO_{2.82}$ and which is structurally isotype to $SrFeO_{2.875}$.

Even though there is still some doubt about the real symmetry and space groups of the intermediate phases, the structural evolution with the uptake of additional oxygen atoms in $SrCoO_{2.5}$ principally goes along with the formation of square planar bipyramidal units and the subsequent formation of rows of corner-sharing octahedra.

3.5. Evolution of the Magnetism during the Oxygen Intercalation. The magnetic properties of non-stoichiometric perovskites have been widely investigated,[34−37] and in this regard, neutron techniques have been among the most informative.[34,35,38]

Since the simultaneous intercalation of 0.5 oxygen atom and release of one electron transforms the antiferromagnetically ordered $SrCoO_{2.5}$ into a ferromagnetically ordered metal $SrCoO_{3.00}$ with a Curie temperature $T_c \approx 300$ °C, neutron diffraction is adequate to study any electronic, i.e., magnetic modifications. The oxidation reaction formally implies the change from Co^{3+} to Co^{4+}, and it is surprising to find such high magnetic correlations in $SrCoO_{2.5}$ with brownmillerite-type structure, since Co^{3+} ($3d^6$) usually adopts an $S = 0$ low-spin state, like in the perovskite $LaCoO_3$.[8] Any modification in the magnetic properties of the brownmillerite can be monitored directly in the relative intensity ratio of the (120)/(021) reflections, which are of purely magnetic origin, as they are forbidden in the two *I*-centered space groups *Imma* and *I*2*mb* but also for *Pnma* concerning nuclear intensities. We have carried out the electrochemical oxidation of $SrCoO_{2.5}$ as described above. In order to be able to resolve the two magnetic reflection intensities, which appear at very similar *d*-values, we have taken advantage of the long wavelength of 4.75 Å, available on the two-axis diffractometer G6.1 at the LLB. This experiment is very sensitive to any modification of the magnetic structure of $SrCoO_{2.5}$, which would immediately cause significant changes in the relative intensity ratio of the (120)/(021) reflection doublet, as all magnetic moments are aligned parallel to the *a*-axis, resulting in a G-type antiferromagnetically orderd structure.[8] Figure 9 shows the evolution of the magnetic doublet (120)/(021) of $SrCoO_{2.5}$ vs *n*. We can establish that neither the cell parameters nor the relative intensity ratio between the two reflections changes during the oxidation of $SrCoO_{2.5}$. The disappearance of the magnetic doublet, as presented in Figure 9, has a linear dependence on the charge-transfer value *n*,

(35) Cussen, E. J.; Vente, J. F.; Battle, P. D. *J. Am. Chem. Soc.* **1999**, *121*, 3958−3967.
(36) Stitzer, K. E.; Smith, M. D.; Gemmill, W. R.; zur Loye, H. C. *J. Am. Chem. Soc.* **2002**, *124*, 13877−13885.
(37) Azuma, M.; Takata, K.; Saito, T.; Ishiwata, S.; Shimakawa, Y.; Takano, M. *J. Am. Chem. Soc.* **2005**, *127*, 8889−8892.
(38) Battle, P. D.; Blundell, S. J.; Brooks, M. L.; Hervieu, M.; Kapusta, C.; Lancaster, T.; Nair, S. P.; Oates, C. J.; Pratt, F. L.; Rosseinsky, M. J.; Ruiz-Bustos, R.; Sikora, M.; Steer, C. A. *J. Am. Chem. Soc.* **2004**, *126*, 12517−12527.

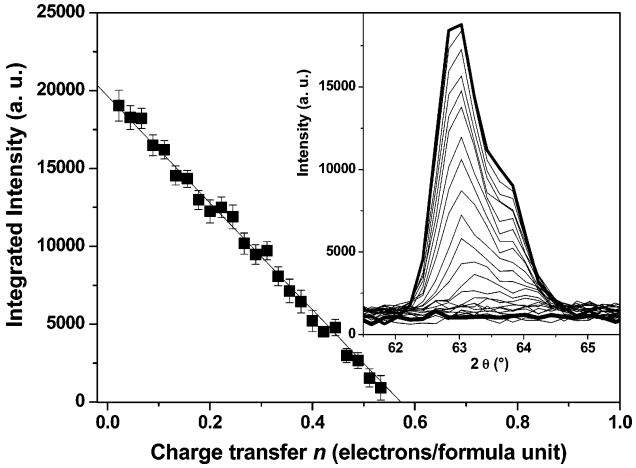

Figure 9. Evolution of the integrated intensities of the purely magnetic doublet (120/021) during the electrochemical oxidation of the electrode $SrCoO_{2.5}$ for $0.0 < n < 0.5$. (Inset) The doublet, where the bold curves represents the patterns collected at $n = 0.0$ and $n = 0.5$. The integrated intensities of the doublet decrease linearly (main part) without any changes in terms of the unit cell parameter or even the intensity ratio between the two reflections (inset).

and the relative ratio of the two reflections remained constant on oxidation. These results confirm that no magnetic modification occurs for the starting phase $SrCoO_{2.5}$; the extra half electron is directly involved in the formation of the new $SrCoO_{2.75}$ phase.

3.6. In Situ EXAFS. Due to its atomic selectivity, X-ray absorption, both in the EXAFS and XANES regions, has been widely employed to investigate the local geometry and the average coordination and valence state of transition metal elements hosted inside non-stoichiometric perovskites.[24,39−47] Most of these studies refers to ex situ experiments, and only very recently have the coordination and oxidation states of iron during the charge and discharge of the $LiFePO_4$ electrodes[24] at current densities typically used in Li ion batteries been investigated in situ. Due to the low *Z* of the atomic species, the $LiFePO_4$ material represents the ideal candidate for such in situ experiments. Here we present, for the first time, an in situ experiment that is able to follow the oxidation process of a highly absorbing material such as $SrCoO_{2.5+\delta}$.

3.6.1. Qualitative Description of in Situ EXAFS and XANES Data. The raw experimental data of the in situ X-ray absorption experiment during the oxidation process are shown in Figure 10a, just after pre-edge subtraction and edge-jump normalization. The first spectrum, corresponding to the $SrCoO_{2.5}$ phase, is presented as a continuous bold line, while the last one, corresponding to the $SrCoO_{3.0}$ phase, is reproduced with a scattered bold line. A selection of the intermediate spectra is depicted using continuous light gray curves. The main part of Figure 10a shows the XANES region (7707−7750 eV), while the first part of the extended region of the normalized μx spectra is given in the inset (7740−8020 eV).

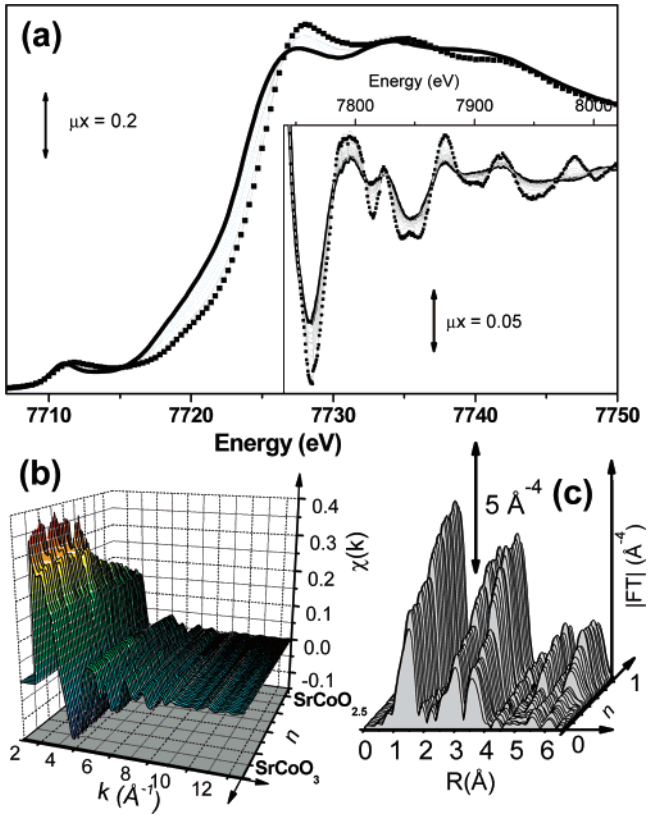

Figure 10. (a) Normalized μx function sampled across the Co K-edge (XANES region) during the oxidation process: starting curve, continuous bold line, corresponding to the $SrCoO_{2.5}$ phase; final curve, scattered bold line, corresponding to the $SrCoO_{3.0}$ phase; selection of the intermediate curves, continuous light gray lines, corresponding to the average $SrCoO_{2.5+x}$ stoichiometry. The blue shift of both pre-edge peak and edge positions, as well as the changes in the white line feature, occurring during the in situ oxidation process are evident. (Inset) The same spectra in the extended region above the edge. (b) Evolution of the $\chi(k)$ functions extracted from the absorption data reported in part (a); curves are plotted in the 2−12.65 $Å^{-1}$ range. The back spectrum corresponds to the starting $SrCoO_{2.5}$ phase, while the front one represents the final $SrCoO_{3.0}$ perovskite phase. The effect of the oxidation is a significant increase of the overall intensity of the $\chi(k)$ functions, mainly due to an increase in the degree of order around the cobalt atoms. (c) Evolution of the k^3-weighted, phase-uncorrected Fourier transform of the $\chi(k)$ functions shown in part (b) (note that here the orientation of the oxidation axis is reversed for graphical reasons: front spectrum, $SrCoO_{2.5}$ phase; back spectrum, $SrCoO_{3.0}$ perovskite phase). The increase in order observed in the $\chi(k)$ functions along the oxidation process, part (b), is well visible also in the corresponding Fourier transforms. This ordering phenomenon is observed in the entire *R* range reported. Of particular interest is the 4.5−6.6 Å region, where the Fourier transform signal is within the noise level in the first stages of the experiments, growing progressively as a function of the evolution of the oxidation process.

The XANES part of the spectrum clearly indicates a blue shift by about 2.0 eV of the edge position, accompanied by a progressive increase of the white line (first resonance after the edge) intensity of 0.09 normalized μx unit, from 1.13 to 1.22. The former feature reflects the increase in the average oxidation state of cobalt during the electrochemical process, while the latter testifies to an increase in the average coordination state of the absorbing atom[48] (Co in this case). In the pre-edge region,

(39) Choy, J. H.; Kim, D. K.; Hwang, S. H.; Demazeau, G.; Jung, D. Y. *J. Am. Chem. Soc.* **1995**, *117*, 8557−8566.
(40) Saini, N. L.; Lanzara, A.; Bianconi, A.; Chou, F. C.; Johnston, D. C. *J. Phys. Soc. Jpn.* **1998**, *67*, 16−19.
(41) Porta, P.; De Rossi, S.; Faticanti, M.; Minelli, G.; Pettiti, I.; Lisi, L.; Turco, M. *J. Solid State Chem.* **1999**, *146*, 291−304.
(42) Subias, G.; Garcia, J.; Blasco, J.; Sanchez, M. C.; Proietti, M. G. *J. Phys.-Condes. Matter* **2002**, *14*, 5017−5033.
(43) Deb, A.; Bergmann, U.; Cairns, E. J.; Cramer, S. P. *J. Phys. Chem. B* **2004**, *108*, 7046−7049.
(44) Haas, O.; Struis, R. P. W. J.; McBreen, J. M. *J. Solid State Chem.* **2004**, *177*, 1000−1010.
(45) Truccato, M.; Lamberti, C.; Prestipino, C.; Agostino, A. *Appl. Phys. Lett.* **2005**, *86*, Art. No. 213116.
(46) Yang, D. S.; Kim, I.; Ulyanov, A. N.; Phan, T. L.; Yu, S. C. *J. Phys. Soc. Jpn.* **2005**, *74*, 2347−2350.
(47) Ra, W.; Nakayama, M.; Cho, W.; Wakihara, M.; Uchimoto, Y. *Phys. Chem. Chem. Phys.* **2006**, *8*, 882−889.

the dipole-forbidden 1s → 3d transition shifts from 7711.0 to 7711.9 eV, with a weak intensity increase and a significant broadening in the high-energy tail of the peak upon moving from the $SrCoO_{2.5}$ phase to the $SrCoO_{3.0}$ phase. By looking at the overall set of spectra in the extended region (see inset), a large number of isosbestic points (points where the intensity of all spectra of the series is the same) is observed: 7715.2, 7726.6, 7781.6, and 7808.6 eV, etc. This is an elegant spectroscopic proof that the $SrCoO_{2.5}$ phase is transforming progressively into the $SrCoO_{3.0}$ phase. Well-defined isosbestic points are routinely observed in high-quality IR experiments[49] but are very rare in X-ray absorption spectroscopy.[23]

The evolution of the $\chi(k)$ functions extracted from the absorption data reported in the inset of Figure 10a is shown in Figure 10b in the 2.00−12.65 $Å^{-1}$ range. The effect of the oxidation causes a significant increase in the overall intensity of the $\chi(k)$ functions. This fact was already appreciable for the raw μx spectra shown in the inset of Figure 10a, but here it is much more evident. Three main factors can lead to an increase in the intensities of the $\chi(k)$ oscillations:[48a−c] (i) an increase in the average coordination number around Co; (ii) a decrease in the dynamic Co−O Debye−Waller factor, reflecting a strengthening of the Co−O bond; and (iii) an increase in the degree of order around cobalt, which causes a decrease in the static part of the EXAFS Debye−Waller factor. Point (i) must play a role, as during the electrochemical oxidation we are introducing oxygen atoms in the lattice, progressively transforming all tetrahedral Co sites (four-fold-coordinated) to octahedral ones (six-fold-coordinated). Point (iii) is also expected to play an important role, as the final $SrCoO_{3.0}$ phase exhibits only almost perfect octahedral sites (with a single first-shell Co−O distance at 1.92 Å), while the $SrCoO_{2.5}$ brownmillerite phase exhibits half of the Co in a strongly distorted octahedral geometry (four planar Co−O distances at 1.92 Å and two axial Co−O distances at 2.20 Å) and the remaining half in a strongly distorted tetrahedral environment (with Co−O distances in the 1.84−1.96 Å range).

The k^3-weighted Fourier transform of the $\chi(k)$ spectra, shown in Figure 10c, clearly supports what was discussed above in terms of the strong increase in the first coordination shell along the oxidation experiment. The data in Figure 10c allow us to go one step further in the conclusions obtained from the EXAFS experiment. In fact, the EXAFS signal of the starting $SrCoO_{2.5}$ phase exhibits well-defined contributions up to 4 Å, while at higher R values no constructive contribution is observed above the noise level (see the first curve in Figure 10c). Along the oxidation process, we do not just observe a progressive increase of the three peaks in the 0.7−4.0 Å range, but we also observe the appearance of four new and well-defined features in the 4.5−6.6 Å region. It is not common to observe such strong EXAFS contributions for such large R values. This fact is direct proof of the high degree of order (on the local ground) of the $SrCoO_{3.0}$ perovskite phase, not present in the initial $SrCoO_{2.5}$ brownmillerite phase.

3.6.2. Quantitative Analysis of the in Situ EXAFS and XANES Data and Comparison with the Parallel NPD Results. The first step in the quantitative analysis of the EXAFS data has been the reproduction of the experimental EXAFS signals of the final $SrCoO_{3.0}$ perovskite and of the initial $SrCoO_{2.5}$ brownmillerite compounds using the theoretical phases and amplitude signals generated by FEFF8 code[50] on clusters constructed from the structure obtained from diffraction refinements (section 3.2). For homogeneity reasons, the simulations have been performed on both systems by reproducing the most relevant single-scattering and multiple-scattering paths within a global path length of 8.0 Å, corresponding to a bond length of 4.0 Å for single-scattering paths. The experimental EXAFS signal of the $SrCoO_{3.0}$ perovskite phase has been perfectly reproduced in a straightforward manner from the fixed geometry given by diffraction data, optimizing only Debye−Waller factors and a single ΔE parameter. Conversely, more delicate has been the reproduction of the starting $SrCoO_{2.5}$ system, for which unusually large Debye−Waller factors have been obtained, reflecting the higher degree of disorder of the brownmillerite phases.

Before starting to analyze the intermediate spectra, it is worth recalling the local nature of the information that can be extracted from EXAFS and XANES, which complement the long-range order-based information obtained from NPD (see section 3.2, where we learned that in the $0.0 < n < 0.5$ region the $SrCoO_{2.5}$ and $SrCoO_{2.75}$ phases coexist, while in the $0.5 < n < 1.0$ region we have basically a single $SrCoO_{2.5+n/2}$ phase). Being able to reveal the average changes occurring only few angstroms around Co atoms, EXAFS will basically monitor the progressive transformation of tetrahedra into octahedra through pyramids occurring upon oxygen intercalation, without being able to discriminate whether this transformation results in one or more ordered phases. From a simple inspection of the inset in Figure 10a, the high number of isosbestic points, as well as their prefect definition, implies that X-ray absorption spectroscopy is basically observing the transformation of a phase A into a phase B. This means that a simpler model must be adopted for analyzing the EXAFS and XANES data.

We then simulated the generic ith experimental spectrum of the in situ experiment as the linear combination of the two reference spectra of the $SrCoO_{3.0}$ perovskite phase [$EXAFS^{Ox}(E_j)$] and of the $SrCoO_{2.5}$ brownmillerite phase [$EXAFS^{Red}(E_j)$]:

$$EXAFS_i^{Theo}(R_j, x_i^{Red}, y_i^{Ox}) = x_i^{Red}\, EXAFS^{Red}(R_j) + y_i^{Ox}\, EXAFS^{Ox}(R_j) \quad (3)$$

where R_j ($j = 1, 2, 3, ..., N$) are the R values where the experimental spectra shown in Figure 10c have been computed with a discrete Fourier transform approach, and x_i^{Red} and y_i^{Ox} are the fractions of $SrCoO_{2.5}$ brownmillerite and $SrCoO_{3.0}$ perovskite phases, respectively. The latter two parameters are optimized by standard least-squares methods, minimizing the function $F(x_i^{Red}, y_i^{Ox})$, defined as

(48) (a) Berlier, G.; Spoto, G.; Bordiga, S.; Ricchiardi, G.; Fisicaro, P.; Zecchina, A.; Rossetti, I.; Selli, E.; Forni, L.; Giamello, E.; Lamberti, C. *J. Catal.* **2002**, *208*, 64−82. (b) Berlier, G.; Spoto, G.; Fisicaro, P.; Bordiga, S.; Zecchina, A.; Giamello, E.; Lamberti, C. *Microchem. J.* **2002**, *71*, 101−116. (c) Bordiga, S.; Damin, A.; Bonino, F.; Zecchina, A.; Spano, G.; Rivetti, F.; Bolis, V.; Prestipino, C.; Lamberti, C. *J. Phys. Chem. B* **2002**, *106*, 9892−9905. (d) Bonino, F.; Damin, A.; Ricchiardi, G.; Ricci, M.; Spano, G.; D'Aloisio, R.; Zecchina, A.; Lamberti, C.; Prestipino, C.; Bordiga, S. *J. Phys. Chem. B.* **2004**, *108*, 3573−3583.

(49) (a) Zecchina, A.; Scarano, D.; Bordiga, S.; Spoto, G.; Lamberti, C. *Adv. Catal.* **2001**, *46*, 265−397. (b) Groppo, E.; Lamberti, C.; Bordiga, S.; Spoto, G.; Zecchina, A. *Chem. Rev.* **2005**, *105*, 115−187.

(50) Ankudinov, A. L.; Ravel, B.; Rehr, J. J.; Conradson, S. D. *Phys. Rev. B* **1998**, *58*, 7565−7576.

$$F(x_i^{Red},y_i^{Ox}) = \sum_{j=1}^{N}[EXAFS_i^{Exp}(R_j) - EXAFS^{Theo}(R_j,x_i^{Red},y_i^{Ox})]^2 \quad (4)$$

We are thus dealing with a two-parameter fit, where the sum of the fractions x_i^{Red} and y_i^{Ox} is not forced to be equal to 1.00. This means, consequently, that a significant deviation of $x_i^{Red} + y_i^{Ox}$ from 1.0, accompanied by a decrease in the quality of the fit, would imply that the two-phase model is not adequate for reproduction of the experimental data. The circles in Figure 11a represent the optimized x_i^{Red} (full circles) and y_i^{Ox} (open circles) factors for all the EXAFS spectra collected during the in situ experiment. The full circles in Figure 11b represent the $x_i^{Red} + y_i^{Ox}$ sum.

The same approach has been applied to the sequence of XANES spectra (Figure 10a), and the optimized x_i^{Red} and y_i^{Ox} factors are shown in Figure 11a using full and open squares, respectively. A remarkable agreement is obtained for both brownmillerite (full symbols) and perovskite (open symbols) by using both EXAFS (circles) and XANES (squares) data.

Also shown in Figure 11a is the edge position (full line, right ordinate axis) measured at the inflection point. When ad hoc superimposed with the fraction of the perovskite phase (open symbols, left ordinate axis), it is evident that the blue shift of the X-ray absorption edge due to the oxidation process well mirrors the formation of the $SrCoO_{3.0}$ phase.

Coming to the discussion of the data in Figure 11b, we see that the sum $x_i^{Red} + y_i^{Ox}$ obtained from EXAFS data (circles) differs from 1.00 by less than 0.02 for all but three of the spectra. In those three cases, values of $1.00 - (x_i^{Red} + y_i^{Ox})$ of $+0.03$, -0.05, and -0.05 were obtained. Similar conclusions can be drawn from the same sum obtained from XANES data (squares in Figure 11b), which differs from 1.00 by less than 0.01 along the whole set of spectra. The results reported herein give further support to the hypothesis that the average local structure around Co can be interpreted as a progressive evolution from that present in the $SrCoO_{2.5}$ brownmillerite phase to that of the $SrCoO_{3.0}$ perovskite phase. This fact is not surprising as, on the local ground probed by both XANES and EXAFS techniques, we are basically observing a progressive transformation of the tetrahedral CoO_4 present in the starting phase into octahedral CoO_6 units of oxidized phase. The presence of the intermediate phase, observed by diffraction techniques (Figure 5c), is not necessarily visible with this local technique.

Notwithstanding this limitation, a careful inspection of all the experimental data summarized in Figure 11a (x_i^{Red} and y_i^{Ox} factors obtained from both EXAFS and XANES data and edge position) shows that the transformation $Co^{III} \rightarrow Co^{IV}$ is not linear along the whole experiment. A linear evolution of the five experimental parameters presented in Figure 11a is observed in the $0 < n < 0.45$ region. The system then seems to be almost unchanged in the $0.45 < n < 0.65$ region. Finally, in the $0.65 < n < 1.0$ region the five parameters again undergo a variation characterized by greater slopes with respect to those observed in the $0 < n < 0.45$ region. When performing a linear fit of the data in regions 1 and 3, we observe that the absolute value of the angular coefficients of both the oxidized and the reduced fractions in region 3 is almost double that found in region 1.

These observations allow us to tentatively hypothesize the following three-step mechanism for the charge transfer: (i) in the $0 < n < 0.45$ region we observe the expected $Co^{III} \rightarrow Co^{IV} + e^-$ charge transfer; (ii) in the $0.45 < n < 0.65$ region we are dealing with $O^{2-} \rightarrow O^- + e^-$; and (iii) in the final $0.65 < n < 1$ region we are dealing with the simultaneous presence of both $Co^{III} \rightarrow Co^{IV} + e^-$ and $O^- + Co^{III} \rightarrow O^{2-} + Co^{IV}$ charge-transfer transitions.

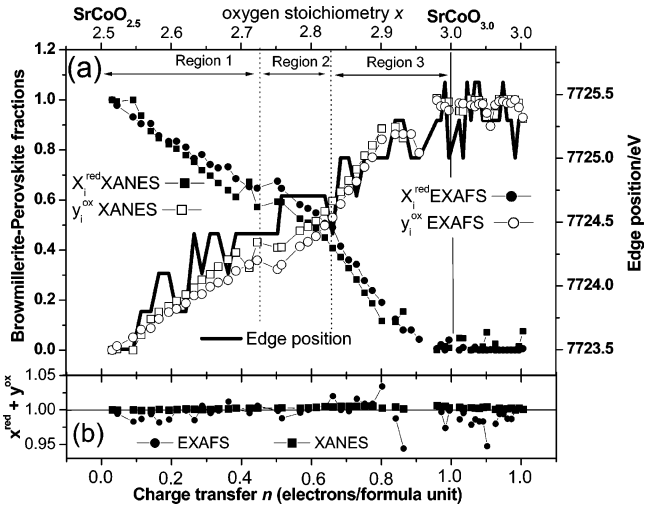

Figure 11. (a). Left axis: evaluation of the reduced (full symbols) and oxidized (open symbols) phases as obtained from the XANES (squares) and EXAFS (circles) data. Right axis: shift of the edge position, which correlates well with the evolution of the oxidized fraction as estimated by both XANES and EXAFS (full line). (b) Sum of the oxidized and reduced fractions as obtained from the XANES (squares) and EXAFS (circles) data. The experimental data in both EXAFS and XANES regions can be perfectly reproduced assuming the presence of two phases only. The vertical full line represents the end of the oxidation run for the $SrCoO_{2.5+x}$ anode; for higher times the stoichiometry does not change from $SrCoO_{3.0}$, and the electron flux just oxidizes the water of the solution. According to the slopes of the oxidation process monitored by both XANES and EXAFS, three different regions have been identified (see vertical dotted lines). This behavior well mirrors the evolution of the electrochemical potential (Figure 3) and that observed in the in situ NPD experiment (see, e.g., Figure 5c).

In this regard, it should be noted that $SrCoO_{2.5+\delta}$ is the first system showing the formation of O^- species during the intercalation reaction. For $La_2NiO_{4+\delta}$, where oxygen can be intercalated on interstitial sites, it has been proven by structural analysis of single-crystal neutron diffraction data, using the maximum entropy method, that the intercalated oxygen must be assumed to be O^{2-}.[51] This interpretation has been confirmed by theoretical calculations on the electronic structure within the density functional theory approach.[52]

We can conclude that the $SrCoO_{2.5} \rightarrow SrCoO_{3.0}$ transformation occurs in a three-region step mechanism, as evidenced independently by electrochemical measurements (Figure 3), in situ NPD (summarized in Figure 5c), and in situ XANES/EXAFS (summarized in Figure 11). Considering that reproducibility problems result from problems related with electric contacts caused by the large volume variation undergone by the electrode during the complete $SrCoO_{2.5} \rightarrow SrCoO_{3.0}$ transformation, the rather good correspondence of the n limits defining the three regions according to the three independent experiments is rather convincing.

(51) (a) Paulus, W.; Cousson, A.; Dhalenne, G.; Berthon, J.; Revcolevschi, A.; Hosoya, S.; Treutmann, W.; Heger, G.; Le Toquin, R. *Solid State Sci.* **2002**, *4*, 565−573. (b) Le Toquin, R.; Paulus, W.; Cousson, A.; Dhalenne, G.; Revcolevschi, A. *Physica B* **2004**, *350*, e269−e272.
(52) Frayret, C.; Villesuzanne, A.; Pouchard, M. *Chem. Mater.* **2005**, *17*, 6538−6544.

4. Concluding Remarks

The most surprising result found during the electrochemical oxidation of $SrCoO_{2.5}$ is the oxygen ordering of the intermediate phase that happens at room temperature. Using a combination of in situ NPD and ex situ synchrotron X-ray diffraction, we were able to characterize the intermediate phases $SrCoO_{2.75}$ and $SrCoO_{2.82\pm0.07}$, and we propose a model of the reaction mechanism on a structural ground that allows the diffusion of oxygen ions into a very dense structure. Using in situ XAFS, we have found a nonlinear evolution of the Co valence state from Co(III) to Co(IV), giving evidence for the formation of O^- species. It thus underlines the extreme complexity of how topotactic solid-state reactions proceed, especially at low temperatures, i.e., far away from thermal equilibrium conditions. In terms of chemical reactivity concerning oxygen intercalation into solid oxides, we must assume a competitive interplay of several parameters, including an appropriate electronic band structure and vacant interstitial or regular lattice sites of the host matrix. In the case of the oxidation of $SrCoO_{2.5}$, the native 1D oxygen vacancy channels in the CoO_4 tetrahedral layers are filled up successively, forming ordered intermediate phases, which involves a change from four-fold tetrahedral coordination to five-fold square pyramidal coordination, finally reaching six-fold octahedral coordination. The capacity of a solid with a densely packed framework to undergo such important structural changes in an ordered way at ambient temperature is quite surprising and should follow a special diffusion mechanism which might be different from typical anion conduction at elevated temperatures. In this way, an adequate band structure also signifies that the sub-bands of the transition metal atoms may directly interfere with the sub-bands of the oxygen atoms on an energetically similar level. The experimental spectroscopic evidence for the formation of O^- species during the intercalation reaction may underline the possible importance of valence state variation or fluctuations between oxygen and the transition metal atoms ($Co^{4+} + O^{2-} \leftrightarrow Co^{3+} + O^-$) for the low-temperature mobility of oxygen in a solid matrix. In this context, it is worth mentioning that the polarizability of oxygen ions may also play a key role for oxygen diffusion in solids.

It is thus clear that the general assumption that a good ionic conductor is always associated with structural disorder phenomena, and that reciprocally all structural disorder may favor any ionic conduction, is questionable when explaining low-temperature oxygen conduction, as complex ordered structures can be involved in the reaction mechanism, as shown for $SrCoO_{2.82\pm0.07}$. Low-temperature ion conduction and especially anion conduction might, however, be restricted to compounds that are able to modify coordination *and* valence states for both cations and anions in a competitive way, thereby reducing considerably the anion radius during each diffusion step, which significantly helps to minimize the activation energy for diffusion processes.

Acknowledgment. This work was supported by Rennes Metropole, the Region Bretagne, and the French Ministry for Education and Research (CPER 2000-06). We acknowledge Drs. Thomas Hansen (D20, ILL Grenoble) and Isabelle Mirebeau (Saclay, CEA) for help during the in situ NPD experiments as well as Dr. Wouter Van Beek from the SNBL BM1B at the ESRF for the synchrotron powder diffraction patterns. We are strongly indebted to S. De Panfilis for having allowed us to make a test few month prior to the in situ XAFS experiment that was critical for optimizing the measuring conditions (sample and electrolyte thickness). Also his support during the experimental work at BM29 is gratefully acknowledged.

Supporting Information Available: Table of structural parameters used for the NPD refinement of the intermediate phase $SrCoO_{2.82}$. This material is available free of charge via the Internet at http://pubs.acs.org.

JA063207M